# ANALYSIS OF STEADY-STATE OPERATION OF HIGH TEMPERATURE HEAT PIPE AND OPTIMIZATION OF THE WORKING MEDIUM

***Yizhuo MENG[1*], Qimeng DUAN[1], Danghua ZHAO[1], Chenxi HOU[1]***

[*1] Department of Chemical Engineering, Northwestern University, Xi'an, 710127, China

[*] Corresponding author; E-mail: 3142632701@qq.com

*High temperature heat pipes exhibit excellent heat transfer performance and can operate stably under high temperature conditions above 750K. They are widely used in heat recovery and heat removal processes. In this paper, a flow and heat transfer model is established to calculate the temperature, pressure, and velocity distribution of the high temperature heat pipe, and the results are similar to the experimental data. In addition, the working medium of the high temperature heat pipe is optimized through a novel optimization method based on probability, and it is concluded that sodium has better heat transfer performance than lithium and potassium under 800K-1000K operating conditions. The optimal result is consistent with the simulation result, which provides a reference for the optimization of working medium in high temperature heat pipes under other operating conditions.*

Key words*: high temperature heat pipe, heat transfer optimization，flow and heat transfer*

## 1. Introduction

High temperature heat pipes(HTHPs) using sodium, potassium, lithium and other metal materials with outstanding thermal conductivity and large latent heat of phase change as the filling medium, could operate stably at more than 750K. HTHP relies on the phase change of metal working medium instead of large temperature gradient to transport a large amount of energy, so it has thermal superconductivity and excellent isothermality, which has a wide range of applications in the waste heat recovery and heat removal processes. The structure of the HTHP is mainly divided into three parts: the vapor region, the wick and the wall, as shown in the Fig. 1. The liquid metal absorbs heat in the evaporation section and evaporates into the vapor region. After that the high temperature vapor reaches the condensation section driven by the pressure gradient, then releases heat and condenses into the wick. And the liquid metal returns to the evaporation section under the capillary pressure in the wick. The heat transfer is realized by this circulation.

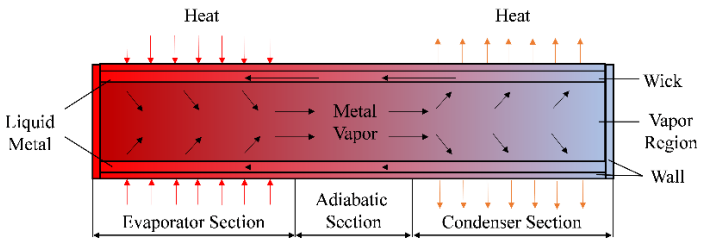


**Fig. 1. The structure and working principle of HTHPs**

For the simulation of the heat transfer process of HTHPs, the lumped model proposed by Faghri et al. [1] obtained the average temperature of the heat pipe in the operation process according to the principle of energy conservation, but could not accurately describe the specific temperature distribution. The thermal resistance network model proposed by Zuo et al. [2] and Tian et al. [3] could accurately describe the temperature distribution of the heat pipe in the operation process, but could not obtain the parameters such as the pressure and flow rate of the working medium inside the heat pipe. In contrast, the flow and heat transfer model calculated the parameters of the heat pipe by restoring the working principle of the heat pipe, which could not only accurately describe the temperature distribution inside and outside the heat pipe, but also reveal the flow rate and pressure distribution of the working medium inside the heat pipe. The model calculates the flow and heat transfer process of the three parts of the HTHP respectively, so as to obtain the accurate temperature, velocity and pressure distribution [4]. Tian et al. [5] coupled the two-dimensional transient heat conduction model of the wall and wick with the one-dimensional quasi-steady compressible vapor flow model to simulate the operation of the heat pipe after the continuous flow was established in the vapor region, and analyzed the influence of the heat transfer power and the working medium on the vapor velocity. Panda et al. [6] built a three-dimensional model to simulate the heat conduction of the wick and wall and the laminar flow and heat transfer of the vapor, obtaining results consistent with the experiment, and analyzed the temperature and velocity distribution of the heat pipe during stable operation. Wang et al. [7] established a flow and heat transfer model similar with Tian et al. [5] to simulate the heat removal performance of the heat pipe in the MSR accident, and verified the heat transfer performance of the high-temperature heat pipe. Han et al. [8] built a two-dimensional axisymmetric steady-state model to simulate the flow and heat transfer in HTHP, obtaining results consistent with the experiment, and gave the distribution of the temperature, pressure and flow rate in the HTHP.

In summary, a large number of existing studies have verified that the flow and heat transfer model could more accurately reflect the temperature, internal pressure, flow rate of the high temperature heat pipe during operation. However, in the existing research, most scholars only analyze the operating characteristics of just one type of high-temperature heat pipe and select high-temperature heat pipes only based on the operating temperature range. But the operating temperature ranges of different high-temperature heat pipes overlap. For example, both potassium heat pipes and sodium heat pipes can operate stably at around 900K. So, selecting the optimal filling medium at the corresponding temperature is a worthwhile research topic. There are few studies on the optimization of the working medium which has a decisive effect on the heat transfer capability. In this paper, the HTHP in steady-state operation is simulated and analyzed by constructing a flow and heat transfer model, and the influence of heat transfer power are analyzed. In addition, consistent with simulation results, the optimal working medium for 800K-1000K operation was selected through a novel optimization method among potassium, sodium, and lithium.

## 2. Models and methods

### 2.1. Flow and heat transfer model of vapor

During steady-state operation, the evaporation and condensation of the working fluid inside the heat pipe remain constant, and the flow rate is relatively uniform. The flow of steam can be regarded

as a two-dimensional axisymmetric compressible laminar flow [9-11]. The governing equations are as follow Eq (1)-(5).

$$\frac{1}{r}\cdot\frac{\partial}{\partial r}(\rho_v v_v)+\frac{\partial}{\partial z}(\rho_v w_v)=0 \tag{1}$$

$$\rho_v\left(v_v\frac{\partial v_v}{\partial r}+w_v\frac{\partial v_v}{\partial z}\right)-\mu_v\left[\frac{\partial^2 v_v}{\partial z^2}+\frac{4}{3}\cdot\frac{1}{r}\cdot\frac{\partial}{\partial r}\left(r\frac{\partial v_v}{\partial r}\right)-\frac{4}{3}\frac{v_v}{r^2}+\frac{1}{3}\frac{\partial^2 w_v}{\partial r\partial z}\right]=-\frac{\partial P_v}{\partial r} \tag{2}$$

$$\rho_v\left(w_v\frac{\partial w_v}{\partial z}+v_v\frac{\partial w_v}{\partial r}\right)-\mu_v\left[-\frac{2}{3}\frac{\partial}{\partial z}\left(\frac{1}{r}\cdot\frac{\partial}{\partial r}(rv_v)\right)+\frac{4}{3}\frac{\partial^2 w_v}{\partial z^2}+\frac{1}{r}\cdot\frac{\partial}{\partial r}\left(r\frac{\partial w_v}{\partial r}\right)+\frac{1}{r}\cdot\frac{\partial}{\partial r}\left(r\frac{\partial v_v}{\partial z}\right)\right]=-\frac{\partial P_v}{\partial z} \tag{3}$$

$$\rho_v\left(w_v\frac{\partial T_v}{\partial z}+v_v\frac{\partial T_v}{\partial r}\right)-\mu_v\frac{k_v}{C_{P,v}}\left[\frac{1}{r}\cdot\frac{\partial}{\partial r}\left(r\frac{\partial T_v}{\partial r}\right)+\frac{\partial^2 T_v}{\partial z^2}\right]=\frac{1}{C_{P,v}}\left(v_v\frac{\partial T_v}{\partial r}+w_v\frac{\partial P_v}{\partial z}+\mu_v\emptyset\right) \tag{4}$$

$$\emptyset=2\left[\left(\frac{\partial v_v}{\partial r}\right)^2+\left(\frac{v_v}{r}\right)^2+\left(\frac{\partial w_v}{\partial z}\right)^2\right]+\left(\frac{\partial v_v}{\partial z}+\frac{\partial w_v}{\partial r}\right)^2-\frac{2}{3}\left[\frac{1}{r}\cdot\frac{\partial}{\partial r}(rv_v)+\frac{\partial w_v}{\partial z}\right]^2 \tag{5}$$

The vapor inside the vapor region is in a high-temperature and low-pressure state, which can be treated as an ideal gas. The equation of state is shown in Eq. (6) [12].

$$P_v=\rho_v\frac{R}{M}T \tag{6}$$

### 2.2. Equivalent thermal conductivity model of wick

HTHPs have high thermal conductivity, and the flow rate of working fluid in the wick is very small. The Pelect number is far less than 1. An equivalent thermal conductivity model can be used to simulate the heat transfer process inside the wick of the heat pipe [13-15]. The equation is given by Eq. (7).

$$k_{eff}\left[\frac{1}{r}\cdot\frac{\partial}{\partial r}\left(r\frac{\partial T_l}{\partial r}\right)+\frac{\partial^2 T_l}{\partial z^2}\right]=0, k_{eff}=\frac{k_l\left(k_l+k_s-(1-\varepsilon)(k_l-k_s)\right)}{k_l-k_s+(1-\varepsilon)(k_l-k_s)} \tag{7}$$

Where the porosity ε could be calculated by the calculation method of the mesh screen type wick [13]. After estimation and calculation, the porosity of the wick in the numerical simulation of this paper is set to 0.8.

### 2.3. Model of the wall

For the pipe wall, only heat transfer needs to be considered, the equation is shown in Eq. (8).

$$k_w\left[\frac{1}{r}\cdot\frac{\partial}{\partial r}\left(r\frac{\partial T_w}{\partial r}\right)+\frac{\partial^2 T_w}{\partial z^2}\right]=0 \tag{8}$$

### 2.4. Boundary condition

#### *2.4.1 Gas-liquid interface*

At the gas-liquid interface, flow is driven by pressure. As shown in the Fig. 2, when the temperature at the gas-liquid interface is higher than the temperature in the vapor region, the saturated vapor pressure at the gas-liquid interface $P_{sat,b}$ is higher than the pressure in the vapor region $P_v$. Assuming the vapor temperature and the temperature of the liquid are equal at the interface, and according to Schrage's kinetic model [16], the flow rate of vapor at the gas-liquid interface $v_{v,b}$ can be calculated by Eq. (9). And the heat flux at the gas-liquid interface can be calculated by Eq. (10). The flow rate of liquid metal leaving the wick at the gas-liquid interface can be calculated using Eq. (11) according to the principle of conservation of mass. The calculation method is the same when the temperature at the gas-liquid interface is lower than the temperature in the vapor region.

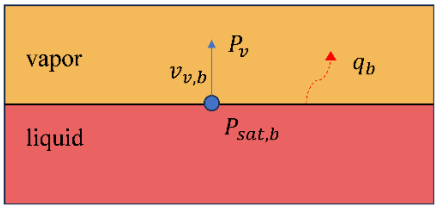


**Fig. 2. Boundary diagram of gas-liquid interface**

$$v_{v,b} = \frac{2\varphi}{(2-\varphi)\rho_v}\sqrt{\frac{M}{2\pi RT_b}}\left(P_{sat,b} - P_v\right) \quad (9)$$

$$q_b = \rho_v v_{v,b} H_{fg} \quad (10)$$

$$v_{l,b} = \frac{\rho_v v_{v,b}}{\rho_l} \quad (11)$$

### *2.4.2 Outer wall boundary*

The boundary conditions of the outer wall of the evaporator section, the adiabatic section and the condenser section are respectively calculated using Eq. (12)-(14). The condenser section is under natural air convection conditions. The axial velocity gradient and temperature gradient at the end face are 0, given by Eq. (15).

$$k_w \frac{\partial T}{\partial r}|_{r=r_{outer}} = \frac{Q_{in}}{S_e} \quad (12)$$

$$k_w \frac{\partial T}{\partial r}|_{r=r_{outer}} = 0 \quad (13)$$

$$k_w \frac{\partial T}{\partial r}|_{r=r_{outer}} = h_c(T - T_{amb}) \quad (14)$$

$$\frac{\partial T}{\partial z}|_{z=l} = \frac{\partial V_v}{\partial z}|_{z=l} = \frac{\partial V_l}{\partial z}|_{z=l} = \frac{\partial T}{\partial z}|_{z=0} = \frac{\partial V_v}{\partial z}|_{z=0} = \frac{\partial V_l}{\partial z}|_{z=0} = 0 \quad (15)$$

### *2.4.3 Central axis boundary*

The radial velocity gradient and temperature gradient at the axis of symmetry are 0, represented by Eq. (16).

$$\frac{\partial T}{\partial r}|_{r=0} = \frac{\partial V_v}{\partial r}|_{r=0} = 0 \quad (16)$$

## 2.5. Grid division and calculation methods

The model mesh division is shown in Fig. 3. A planar quadrilateral mesh is constructed to divide the axisymmetric surface of the heat pipe into elements, and 3 layers of boundary mesh is added at the interface between the vapor region and the wick to refine the mesh here to capture heat and mass transfer phenomena at the interface more accurately.

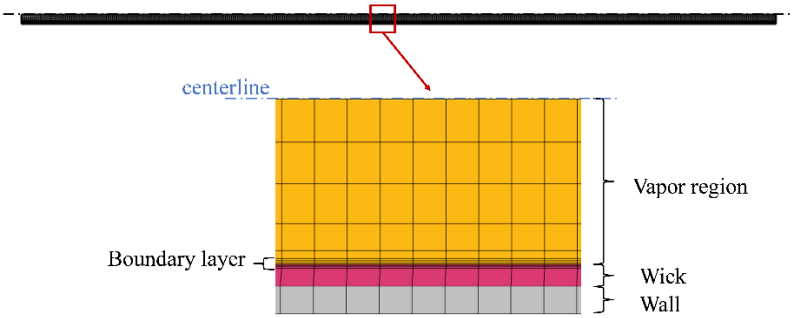


**Fig. 3. Mesh**

The simulation results are independent of the number of grids. With the refinement of the grid and the increase of the number of cells, the calculation results hardly change. For example, the temperature distribution at the centerline of the sodium heat pipe designed in this paper at 1188W heating power calculated under different grid cells number is shown in Fig. 4.

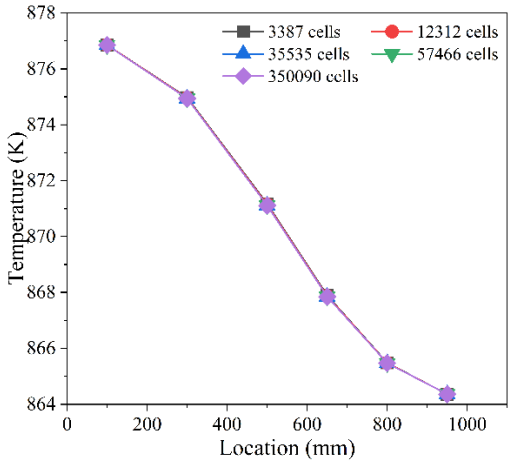


**Fig. 4. Temperature distribution calculated under different grid cells number**

Solve the model using COMSOL Multiphysics software which has a powerful ability to couple multiple physical fields. Using the built-in laminar flow module and heat transfer of porous medium module in the software to couple and solve the flow and heat transfer characteristics inside the heat pipe. Using direct coupling method, i.e. whole field discretization and whole field solution method for calculation [17]. The coupled algorithm has more advantages in dealing with problems involving multi physics field coupling. For the steady-state single-phase problems in the vapor region, the coupled algorithm is more stable and efficient compared to the separation method.

## 3. Models and methods

### 3.1. Model verification

The experimental data obtained by Lee et al. [18] is used to verify the accuracy of the model. Construct a physical model consistent with its experimental process, and the sodium heat pipe characteristic parameters used in the experimental process are shown in Tab. 1.

**Tab. 1. The geometry of the sodium heat pipe**

| item | size | item | size |
|---|---|---|---|
| l | 1m | $l_a$ | 0.15m |
| $r_{outer}$ | 0.0127m | $l_c$ | 0.425m |
| $l_e$ | 0.425m | $t_w$ | 0.00165m |

The wall of the heat pipe and the wick are made of 316L seamless stainless steel, whose density is 7980[kg/m$^3$], heat capacity is 500[J·kg$^{-1}$·K$^{-1}$], thermal conductivity is 16[W·m$^{-1}$·K$^{-1}$].

During the working process of sodium heat pipes, there are three phases of sodium working fluid, and their thermodynamic properties are different and vary with temperature. In order to better fit the actual situation, the thermodynamic properties are calculated by the Eq. (17)-(23) [19].

$$\rho_l = 950.1 - 0.22976t - 1.46 \times 10^{-5}t^2 + 5.638 \times 10^{-9}t^3 \quad (17)$$

$$\mu_l = 0.1\exp(-1.6814 - 0.4296lgT + 234.65/T) \quad (18)$$

$$\mu_v = 6.083 \times 10^{-9}T + 1.2606 \times 10^{-5} \quad (19)$$

$$k_l = 93 - 0.0581t + 1.173 \times 10^{-5}t^2 \quad (20)$$

$$C_{P,l} = 1437.08 - 0.5806t + 4.6239 \times 10^{-4}t^2 \quad (21)$$

$$P_{sat} = 101325 \times 10\text{^}\left(6.354 - \frac{5567}{T} - 0.5lgT\right) \quad (22)$$

$$H_{fg} = 4.63644 \times 10^6 - 180.817T \quad (23)$$

The density of sodium vapor can be calculated by Eq. (6). The viscosity, thermal conductivity, and specific heat capacity are respectively $1.751 \times 10^{-6}$ [Pa·s], 0.0303[W·m$^{-1}$·K$^{-1}$], and 2658.618[J·kg$^{-1}$·K$^{-1}$] according to the operating temperature [19].

Steady state operation simulations were conducted on the sodium heat pipe at constant heating powers of 1188W, 958W, and 696W in the evaporator section. The flow and heat transfer inside the sodium heat pipe during stable operation at 1188W heating power are shown in Fig. 5.

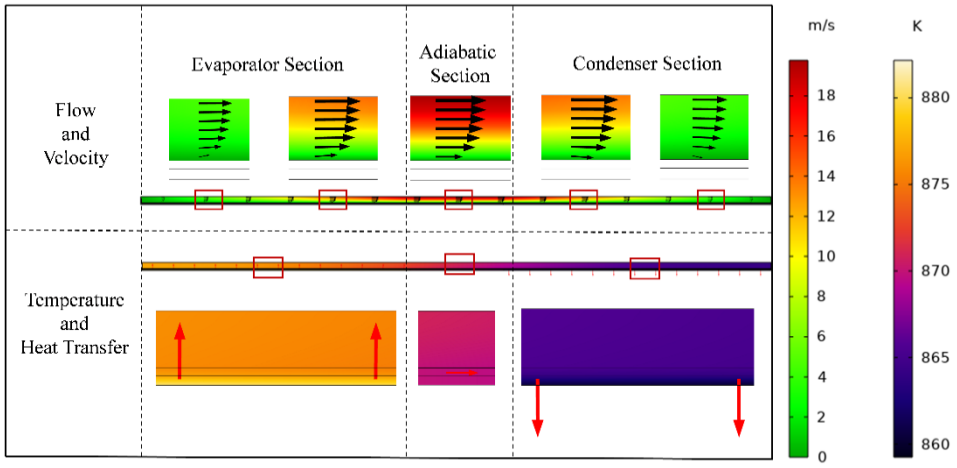


**Fig. 5. Internal flow and heat transfer of sodium heat pipe at 1188W heating power**

The arrow direction on the flow and velocity distribution diagram represents the direction of flow velocity, and its length represents the magnitude of flow velocity. It can be seen that in the evaporator and condenser sections, the sodium vapor flow velocity near the wall is relatively small and has a certain radial velocity component, which reproduces the process of sodium vapor entering the vapor region from the wick and flowing back to the wick in the condenser section. That is, there is flow from the wick into the vapor region in the evaporator section, flow from the vapor region into the wick in the condenser section. But the flow in the adiabatic section remains horizontal. The arrows on the temperature and heat transfer distribution figure represent the direction and magnitude of heat flow. Heat enters the evaporator section from the external heat source and dissipates to outside in the condenser section. In the adiabatic section, due to ignoring heat loss, the heat flow only exists in the axial direction. These are all consistent with the actual behavior during the operation of the heat pipe.

Further verify the simulation accuracy of the model by measuring the temperature distribution in the heat pipe. Take the same temperature measurement points A-F as the experiment, as shown in Fig. 6.

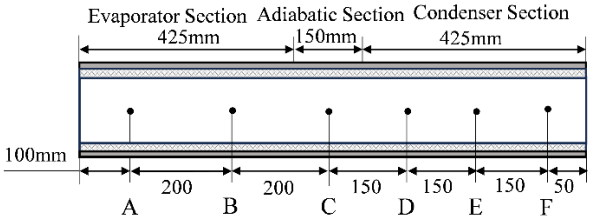


**Fig. 6. Temperature measurement points**

The temperature distribution inside the heat pipe during steady-state operation obtained from simulation and the data obtained from Lee et al.'s experiments are shown in Fig. 7. The average heat flux of the condenser section in the experimental and simulation results under different heating powers is shown in Fig. 8.

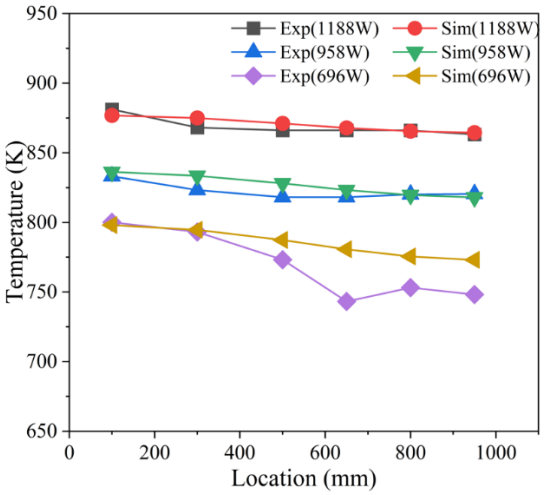


**Fig. 7. Comparison of vapor temperature distribution obtained by simulation and experiments.**

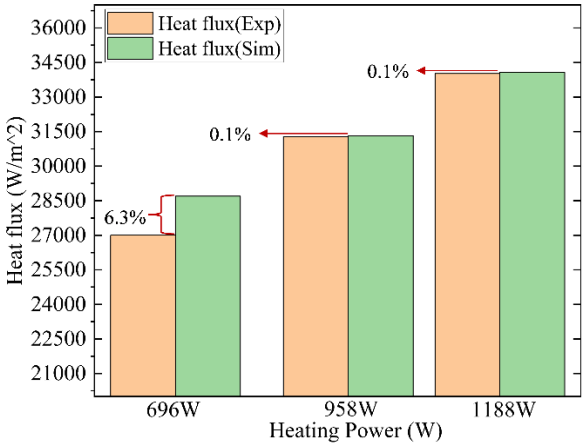


**Fig. 8. The average heat flux of the condenser section**

The average errors of the simulation temperature compared to the experiment are respectively 0.38%, 0.64%, and 2.27% at 1188W, 958W and 696W heating power. The generation of simulation errors is largely due to the neglect of heat loss in the adiabatic section during simulation, which exists under actual conditions. The error of the simulation results compared to the experimental data decreases with the increase of heating power in the evaporator section. Because the higher the heating power, the higher the heat flux density the heat pipe, and the smaller the ratio of the heat flux lost in the adiabatic section to the effective heat flux.

### 3.2. Heat pipe operating characteristic

Calculate the temperature, pressure and velocity distribution on the wall, wick, and vapor region of the sodium heat pipe at heating powers of 1188W, 958W, and 696W respectively. The results are shown as Fig. 9.

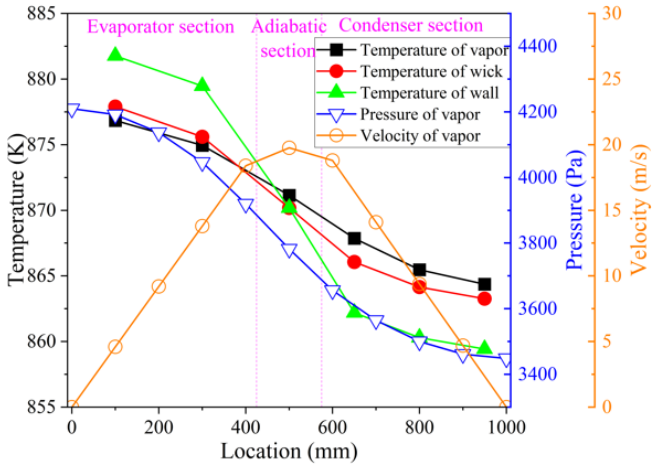


**Fig. 9. (a) Results at 1188W**

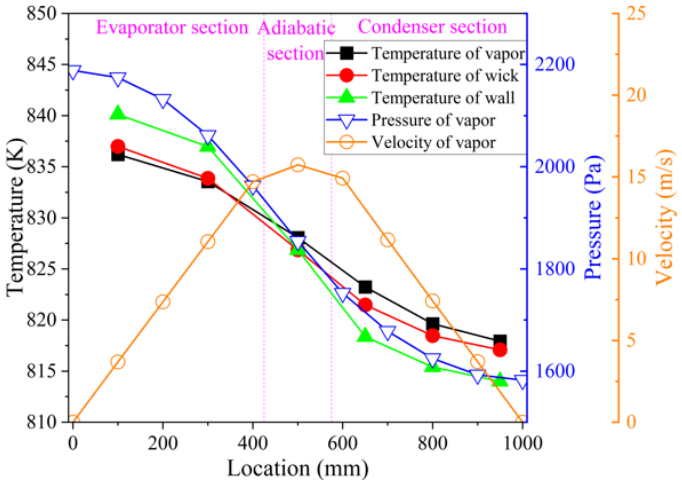


**Fig. 9. (b) Results at 958W**

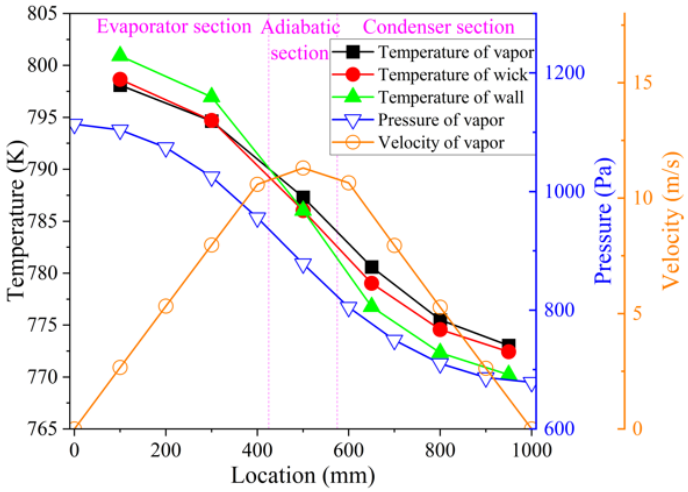


**Fig. 9. (c) Results at 696W**

In the heat conduction process of the heat pipe, the temperature difference of the wall is the largest, followed by the wick, and the vapor region has better isothermality due to the flow and heat

transfer. Because there is no heat input and output in the adiabatic section, the temperature difference of the wall, the wick and the vapor region is smaller. The overall pressure of the vapor in the HTHP increases with the increase of the heating power, and the pressure of the vapor from the evaporator section to the condenser section decreases. Moreover, the difference in the internal pressure of the heat pipe is positively correlated with the heating power, because the higher the heating power is, the higher the overall temperature of the heat pipe is, and the higher the saturated vapor pressure of the metal working medium is. The velocity of the vapor in the heat pipe increases first and then decreases from the evaporator section to the condenser section, and reaches its maximum value in the adiabatic section. Because the temperature difference between the two ends of the area is the largest so that the saturated vapor pressure difference is the largest.

### 3.3. Evaluation and optimization of the working medium

The commonly used working medium of sodium, potassium and lithium are evaluated and optimized for HTHPs at operating temperature 800-1000K. The thermodynamic property of the three materials were evaluated by the multi-objective optimization method based on probability raised by Zheng et al. [20]. And the calculation method is shown in Eq. (24)-(28) [20].

The index of "the bigger the better":

$$\mathrm{p}_{ij} \infty \mathrm{U}_{ij}\ , \mathrm{p}_{ij} = \alpha_j \mathrm{U}_{ij}\ , i = 1,2, \dots, n,\ j = 1,2, \dots, m. \quad (24)$$

$$\sum_{i=1}^{n} \alpha_j \mathrm{U}_{ij} = \sum_{i=1}^{n} \mathrm{p}_{ij} = 1,\ \ \alpha_j = 1/(n\bar{\mathrm{U}}_j) \quad (25)$$

The index of "the smaller the better":

$$\mathrm{p}_{ij} \infty (\mathrm{U}_{jmax} + \mathrm{U}_{jmin} - \mathrm{U}_{ij})\mathrm{p}_{ij} = \beta_j (\mathrm{U}_{jmax} + \mathrm{U}_{jmin} - \mathrm{U}_{ij})\ , i = 1,2, \dots, n,\ j = 1,2, \dots, m. \quad (26)$$

$$\beta_j = 1/[n(\mathrm{U}_{jmax} + \mathrm{U}_{jmin}) - n\bar{\mathrm{U}}_j] \quad (27)$$

$$\mathrm{p}_i = \mathrm{p}_{i1} \cdot \mathrm{p}_{i2} \cdots \mathrm{p}_{im} = \prod_{j=1}^{m} \mathrm{p}_{ij} \quad (28)$$

The density $\rho$, thermal conductivity $k$, heat capacity $C_P$, latent heat of vaporization $H_{fg}$, and the viscosity $\mu_v$ are selected as the evaluation index of heat transfer performance of the HTHPs in this paper. The first four are positive indices, and the greater the value is, the stronger the heat storage and heat transfer ability of the working medium is. The viscosity is a negative index, because the greater the value is, the greater the flow resistance of the metal vapor in the heat pipe is. The thermodynamic properties of potassium are calculated by Eq. (29)-(34) [19,21].

$$\rho_l = 841.5 - 0.2127t - 2.7 \times 10^{-5} t^2 + 4.77 \times 10^{-9} t^3 \quad (29)$$

$$\mu_l = 0.1\exp(-1.1973 - 0.6100 lgT + 159.97/T) \quad (30)$$

$$\mu_v = 6.083 \times 10^{-9} T + 1.2606 \times 10^{-5} \quad (31)$$

$$k_l = 43.8 + 2.22 \times 10^{-2}(T - 273) + 3.95 \times 10^3 / T \quad (32)$$

$$C_{P,l} = 838.9 - 0.36741T + 4.592 \times 10^{-4} T^2 \quad (33)$$

$$P_{sat} = 101325 \times 10\text{^}\left(6.59817 - \frac{4625.3}{T} - 0.700643 lgT\right) \quad (34)$$

The thermodynamic properties of lithium are calculated by Eq. (35)-(40) [19,21].

$$\rho_l = 508.7 - 0.0825 \times (T - 453.15) \quad (35)$$

$$\mu_v = 10\text{^}(-3.08 + \frac{57.63}{T} - 5.172 \times 10^{-4} T) \quad (36)$$

$$k_l = 21.42 + 0.0523T - 1.371 \times 10^{-5} T^2 \quad (37)$$

$$C_{P,l} = 4186.8 \times (0.8429 + 1.885 \times 10^{-4} T - 6.866 \times 10^{-8} T^2 + \frac{297.89}{T}) \quad (38)$$

$$H_{fg} = 4186.8 \times 10^3 \times (5.25 - 3.65 \times 10^{-4} \times T) \quad (39)$$

$$P_{sat} = 100000 \times 10\text{^}(4.98831 - (7918.984/(\mathrm{T} - 9.52))) \quad (40)$$

In summary, the preferable probability of each index of the three working fluids can be derived, such as the preferable probability of the density of sodium, potassium and lithium working fluids can be expressed by Eq. (41)-(43).

$$P_{Na,\rho} = \frac{5.638\times10^{-9}T^3-1.922\times10^{-5}T^2-0.221T+1011.655}{1.041\times10^{-8}T^3-5.013\times10^{-5}T^2-0.501T+2455.227} \quad (41)$$

$$P_{K,\rho} = \frac{4.77\times10^{-9}T^3-3.091\times10^{-5}T^2-0.197T+897.487}{1.041\times10^{-8}T^3-5.013\times10^{-5}T^2-0.501T+2455.227} \quad (42)$$

$$P_{Li,\rho} = \frac{546.085-0.0825T}{1.041\times10^{-8}T^3-5.013\times10^{-5}T^2-0.501T+2455.227} \quad (43)$$

Similarly, the preferable probability expressions of thermal conductivity, heat capacity and latent heat of vaporization phase transition of the three working fluids can be expressed.

The viscosity of gaseous working medium changes little with temperature. Here, the preferable probability is calculated by Eq. (27) and Eq. (28) under 900K, as follow: $P_{Na,\mu_v}$=0.48910；$P_{K,\mu_v}$=0.48659；$P_{Li,\mu_v}$=0.02431.

The overall preferable probability of sodium, potassium and lithium can be expressed by Eq. (44), such as the overall optimization probability of sodium.

$$P_{Na} = P_{Na,\rho} * P_{Na,k} * P_{Na,C_P} * P_{Na,\mathrm{hl}} * P_{Na,\mu_v} \quad (44)$$

The overall preferable probability at 800-1000K is shown in Fig. 10.

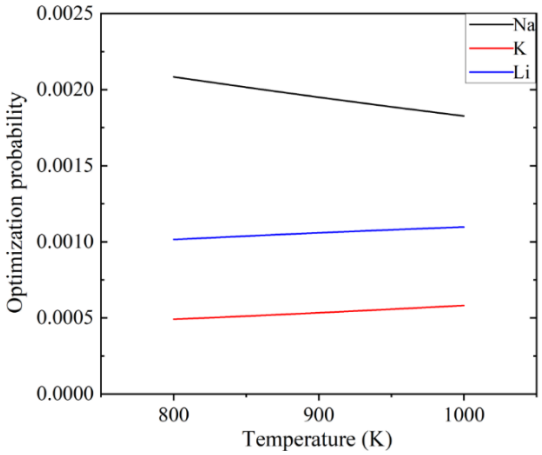


**Fig. 10. The overall preferable probability of sodium, potassium and lithium**

Under the same heating power, the simulated temperature distribution of wall of sodium, potassium and lithium heat pipes of the same size and structure are shown in Fig. 11.

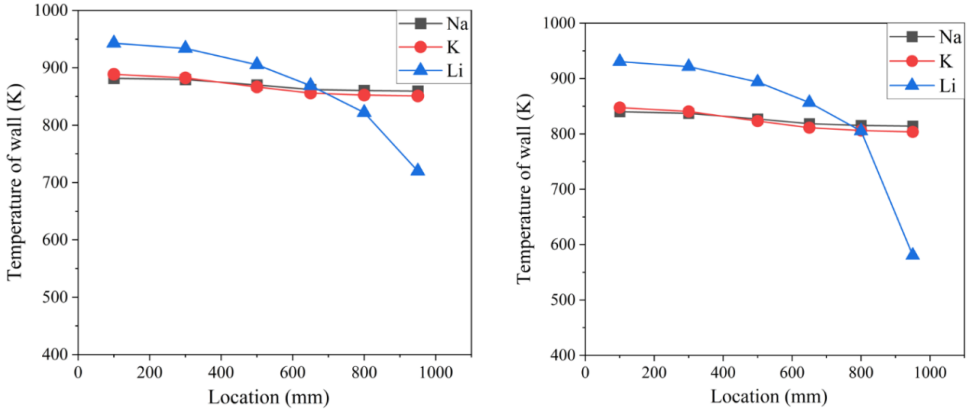


**Fig. 11. (a) Temperature distribution of wall at 1188W (b) Temperature distribution of wall at 958W**

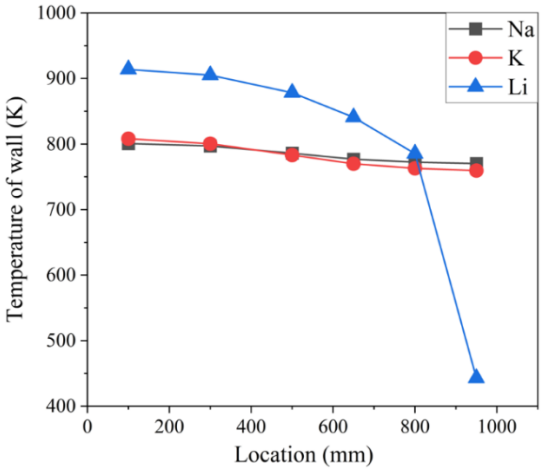


**Fig. 11. (c) Temperature distribution of wall at 696W**

Under the same heating powers of 1188W, 958W and 696W, the wall of sodium heat pipe has the best isothermality, so the heat flux of the condenser section is the largest at the same external temperature, the overall heat transfer power is higher, which is consistent with the optimization results mentioned above. However, the temperature difference of lithium heat pipe is large and the lower the heating power is, the greater the difference is, because the lithium heat pipe is not fully started under 800-1000K.

According to the research of Tian et al. [5] and Zhang et al. [22], the state transition temperature of lithium vapor is above 1000K when the diameter of the vapor region is about 20mm, and the state transition temperature of potassium and sodium is below 750K. Therefore, the temperature of the lithium heat pipe does not reach the state transition temperature of lithium vapor flow, and there is no continuous vapor flow in the vapor region. As shown in Fig. 12, lithium vapor has been completely condensed before reaching the end of the condenser section. The efficiency of heat transfer from the evaporator section to the condenser section decreases, which divides the heat pipe into a hot region and a cold region. The heat transfer between the two regions still mostly carried out through the heat conduction of the pipe wall, so its isothermality is poor.

In summary, at an operating temperature of 800-1000K, sodium should be selected as the working medium among sodium, potassium and lithium which has higher heat discharge power under the same heating conditions, that is, it has higher heat transfer power under the same working temperature.

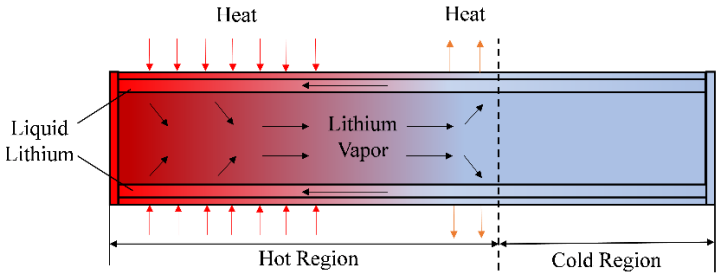


**Fig. 12. Partially started lithium heat pipe**

Under the same heating power of 1188W, the pressure and velocity distribution of potassium, sodium and lithium heat pipes is shown in Fig. 13.

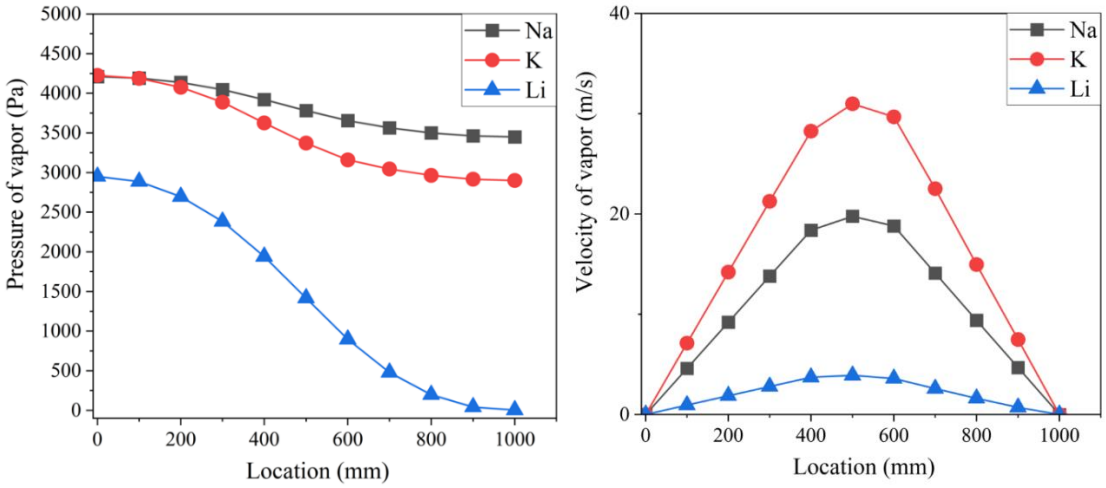


**Fig. 13. (a) Vapor pressure distribution at 1188W (b) Vapor velocity distribution at 1188W**

Under the same heating power, the pressure of the sodium heat pipe is higher than that of the potassium heat pipe, but the pressure difference of the potassium heat pipe is larger than that of the sodium heat pipe, which makes the flow velocity higher. The continuous vapor is not formed in the lithium heat pipe, a small amount of lithium steam has been completely condensed before reaching the end of the condensation section, which makes the internal pressure of the lithium heat pipe lower and tends to zero at the end of the condensation section, and the flow velocity of the lithium steam is extremely low. So, at this time, it is difficult for the working medium lithium to transfer heat to the condensation section through flow heat transfer in the vapor region.

The above discussion suggests that the potential operating range of the high-temperature heat pipe is within the range where the working medium forms a continuous flow. For example, lithium cannot be used as the working medium at temperatures below 1000K when the diameter of the vapor region is about 20mm.

## 4. Conclusion

A steady-state heat transfer simulation model of the heat pipe is constructed to simulate the working process of the HTHPs, and the results are similar to the experimental data. The internal vapor flow rate, pressure and temperature distribution of each part of the heat pipe which are difficult to measure in experiments are calculated and analyzed, and the heat transfer performance of three kinds of working medium is analyzed and optimized. The following conclusions are drawn:

(1) The overall pressure of the steam in the HTHPs increases with the increase of the heating power, and the pressure from the evaporator section to the condenser section decreases, and the vapor pressure difference in the heat pipe is positively correlated with the heating power. It's because the saturated vapor pressure of the working medium increases with the increase of temperature.

(2) The vapor velocity in the heat pipe from the evaporator section to the condenser section shows a trend of increasing first and then decreasing, and the velocity reaches the maximum in the adiabatic section. It's because the temperature difference between the two ends of the adiabatic section is the largest in the heat pipe, and the saturated vapor pressure difference of the metal working medium is the largest.

(3) The evaluation results of the optimization method based on probability are consistent with the simulation results, that is, when considering the heat transfer power, sodium should be selected as

the working medium among sodium, potassium and lithium at 800-1000K, which has higher heat transfer power at the same working temperature between 800-1000K. This provides a reference for the optimization method of the working medium of HTHPs at other temperatures. At the same heating power, the pressure in the sodium heat pipe is higher than that of the potassium heat pipe, but the pressure difference of the potassium heat pipe is higher, which makes the velocity higher. However, the lithium heat pipe vapor region does not form continuous flow, so it is difficult transfer heat to the condenser section. Therefore, a premise for selecting working medium for the HTHP under certain working conditions is that the medium vapor can form continuous flow under that working condition.

**Nomenclature**

Nomenclature

| | | | |
|---|---|---|---|
| $C$ | Specific Heat Capacity [J·kg$^{-1}$·K$^{-1}$] | $\beta$ | Normalization factor of negative index [-] |
| $H_{fg}$ | Latent heat of vaporization [J/kg] | $\rho$ | Material density [kg·m$^{-3}$] |
| h | Heat transfer coefficient [W·m$^{-2}$·K$^{-1}$] | $\mu$ | Dynamic viscosity [Pa·s] |
| $k$ | Heat conductivity [W·m$^{-1}$·K$^{-1}$] | ε | Porosity of wick [-] |
| $l$ | Length [m] | $\emptyset$ | Source term [-] |
| $M$ | Molar mass [kg·mol$^{-1}$] | $\varphi$ | Regulatory factor [-] |
| $P$ | Pressure [Pa] | Subscripts | |
| p | Preferable probability | $a$ | Adiabatic section |
| $Q_{in}$ | Heating power[W] | $amb$ | Ambient |
| $q$ | Heat flux[W·m$^{-2}$] | b | Liquid-vapor interface |
| $R$ | gas constant [8.314 J·mol$^{-1}$·K$^{-1}$] | $c$ | Condensation section |
| $r$ | Radial position [m] | e | Evaporation section |
| S | Area [m$^2$] | eff | Effective |
| $T$ | Temperature [K] | $i$ | object "$i$" |
| $t$ | Temperature [℃] | $j$ | index "$j$" |
| $t_w$ | Wall thickness[m] | $l$ | Liquid |
| U | The value of the index [-] | $max$ | Maximum value |
| $\overline{U}$ | The average value of the index [-] | $min$ | Minimum value |
| $V$ | Velocity [m/s] | s | Porous matrix |
| $v$ | Radial velocity [m/s] | sat | Saturation |
| w | Axial velocity [m/s] | $v$ | Vapor |
| $z$ | Axial position [m] | $w$ | Wall |

Greek symbols

| | |
|---|---|
| α | Normalization factor of the positive index [-] |

**References**

[1] Faghri, A., *et al.*, Transient Lumped Heat-Pipe Analyses, *Heat Recovery Systems & CHP*, *14*(1999),4, pp. 351-363.

[2] Zuo, Z. J., Faghri, A., A Network Thermodynamic Analysis of the Heat Pipe. *International Journal of Heat and Mass Transfer*, *41*(1998), 11, pp. 1473-1484.

[3] Tian, Z, X., *et al.*, Study on Heat Transfer Performance of High Temperature Potassium Heat Pipe at Steady State, *Atomic Energy Science and Technology*, *54*(2020), 10, pp. 1771-1778.

[4] Tian, Z, X., *et al.*, A Review of Liquid Metal High Temperature Heat Pipes: Theoretical Model, Design, and Application, *International Journal of Heat and Mass Transfer*, *214*(2023), 0, pp.124434.

[5] Tian, Z, X., *et al.*, Code Development and Analysis on the Operation of Liquid Metal High Temperature Heat Pipes under Full Condition, *Annals of Nuclear Energy*, *160*(2021), 0, pp.108396.

[6] Panda, K. K., *et al.*, Numerical Simulation of High Temperature Sodium Heat Pipe for Passive Heat Removal in Nuclear Reactors, *Nuclear Engineering and Design*, *323*(2017), 1, pp.376-385.

[7] Wang, C. L., *et al.*, Study on the Characteristics of the Sodium Heat Pipe in Passive Residual Heat Removal System of Molten Salt Reactor (Article), *Nuclear Engineering and Design*, *265*(2013), 0, pp. 691-700.

[8] Han, Y., *et al.*, Numerical simulation of potassium heat pipe based on porous media model, *Atomic Energy Science and Technology*, *48*(2014), 1, pp.49-53.

[9] Zhang, H., *et al.*, *Re Guan Jie Neng Ji Shu* (Energy Saving Technology for Heat Pipes, Chinese). Chemical Industry Press, Beijing, China, 2009.

[10] Bowman, W. J., Hitchcock, J. E., Transient compressible heat-pipe vapor dynamics, *Proceedings*, Proceedings of the 25th ASME National Heat Transfer Conference. New York, USA, 1988, pp. 329-337.

[11] Jiao, G. H., *et al.*, Flow Heat Transfer and Mechanical Characteristics of High Temperature Heat Pipe Based on Multi-physics Coupling, *Annals of Nuclear Energy*, *58*(2024),1, pp. 60-68.

[12] Shen, W. D., *et al.*, *Gong Cheng Re Li Xue* (Engineering Thermodynamics, Chinese), Higher Education Press, Beijing, China, 2016.

[13] Faghri, A., *et al*., *Heat Pipe Science and Technology*, Taylor & Francis, Oxford, UK, 1995.

[14] Chi, S. W., *et al.*, *Heat Pipe Theory and Practice: A Sourcebook*, Hemisphere Pub Corp, Washington, USA, 1976.

[15] Liu, W., *et al.*, *Duo Kong Jie Zhi Chuan Re Chuan Zhi Li Lun Yu Ying Yong* (Theory and Application of Heat and Mass Transfer in Porous Media, Chinese), Science Press, Beijing, China, 2006.

[16] Schrage, R. W., *et al.*, *A Theoretical Study of Interface Mass Transfer*, Columbia University Press, New York, USA, 1953.

[17] Tao W. Q., *et al*., *Shu Zhi Chuan Re Xue* (Numerical Heat Transfer, Chinese), Xi'an Jiaotong University Press, Xi'an, China, 2001.

[18] Lee, B. I., Lee, S. H., Manufacturing and Temperature Measurements of a Sodium Heat Pipe, *KSME International Journal*, *15*(2001), 11, pp. 1533-1540.

[19] Qian, Z. Y. *Di Rong Dian Jin Shu De Re Wu Xing* (Thermophysical Properties of Low Melting Point Metals, Chinese), Science Press, Beijing, China, 1985.

[20] Zheng, M. S., *et al*., *Probability-Based Multi-objective Optimization for Material Selection*, Springer Nature Singapore, 2024.

[21] Hicks, W. T., Evaluation of Vapor & hyphen; Pressure Data for Mercury, Lithium, Sodium, and Potassium, *Journal of Chemical Physics*, *38*(1963), 8, pp: 1873-1880.

[22] Zhang, Z. Q., *et al.*, Numerical Investigation on Startup Characteristics of High Temperature Heat Pipe for Nuclear Reactor, *Nuclear Engineering and Design*, *378*(2021), 0, pp.111180.

Submitted: 30.4.2024
Revised: 26.8.2024
Accepted: 04.9.2024.